Journal of Wood Science

ORIGINAL ARTICLE

Open Access

Mössbauer and Raman characterization of iron-loaded woody charcoal: effects of Fe^{3+}-dispersion in wood on reduction of Fe^{3+} and graphitization in carbonization

Takayuki Yamagishi[1], Shigeru Yamauchi[2*], Sakae Shibutani[2], Hikaru Suzuki[2], Tsutomu Takayama[3] and Yoichi Sakai[3]

Abstract

An Fe^{3+}-impregnation method was improved to disperse Fe^{3+} in wood powder more homogeneously, and the wood powder was carbonized at various temperatures. The obtained iron-loaded charcoal samples were analyzed using Mössbauer and Raman spectroscopy to understand the effects of the improved method on the reduction of Fe^{3+} and graphitization. G′(2D)-band was adopted as a marker of graphitic structure formation among Raman scattering due to sp^2-carbon. Mössbauer and Raman characterization confirmed that the reduction from Fe^{3+} to Fe^0 is closely related with the graphitization in charcoal; however, both the chemical changes progressed rapidly from a much lower temperature-range and graphitization occurred more uniformly compared with charcoal synthesized using the previous method containing no decompression-impregnation processes. Moreover, the effects of holding time at carbonization temperature and Fe^{3+} content in the wood powder were examined in terms of relationship between the reduction of Fe^{3+} and graphitization. It was suggested that there were multiple reaction paths to graphitization in carbonization.

Keywords: Charcoal, Graphitization, Fe^{3+}-dispersion, Mössbauer spectroscopy, Raman spectroscopy

Introduction

The carbon materials have been applied in various scientific and engineering fields because of their diverse electrical or mechanical properties. However, carbon is not an abundant element in the earth's crust. Carbon resources available are limited, and will be seriously depleted by haphazard usage. Woody biomass is not only an alternative energy to fossil fuels, but also a prospective resource for carbon materials.

Nevertheless, research on the utilization of woody biomass as a starting material for functional carbon has not shown sufficient progress, because woody biomass has disadvantages as a raw material for carbon. The carbon content of wood is much smaller than that of petroleum or coal, and wood is difficult to handle chemically, because of its extremely limited solubility in any solvent. Thus, a conventional technique to obtain carbon from woody biomass is heat-treatment free from oxygen at high temperatures, namely, carbonization. T. Suzuki and K. Suzuki revealed that crystallized mesoporous carbon with high electrical conductivity can be produced from wood impregnated with iron(III) or nickel(II) salts even at a temperature lower than 900 °C [1–9], and confirmed that metal-loaded charcoal can contain crystallized carbon nanoshells that link to one another and form chain-like structures. They have proposed that the nanoshell chains should be named "graphite nanoshell chains" [9].

*Correspondence: sigeru@iwt.akita-pu.ac.jp
[2] Institute of Wood Technology, Akita Prefectural University, 11-1 Kaieisaka, Noshiro 016-0876, Japan
Full list of author information is available at the end of the article

We previously reported the Mössbauer and Raman characterization of iron-loaded charcoal made from wood powder Japanese cypress (*Chamaecyparis obtusa*) at various temperatures [10]. As a result, it was found that charcoal samples synthesized at above 850 °C were largely graphitized, and contained metallic iron and Fe_3C as principal iron species, suggesting that the reduction from Fe^{3+} to Fe^0 was closely related with graphitization. However, substantial amounts of amorphous carbon remained even in charcoal synthesized at 900 °C [10]. Thus, we assumed that the amorphous carbon residue was due to poor homogeneity in the dispersion of Fe^{3+} in raw wood powder, and focused on two points to obtain more even dispersion of Fe^{3+} ions. One was the improvement of the impregnation method of Fe^{3+}, and the other was the change from Japanese cypress to wood to be impregnated with Fe^{3+} more readily. In this study, Japanese cedar (*Cryptomeria japonica*) was adopted as a raw woody material instead of Japanese cypress, because Japanese cedar wood is expected to be impregnated with Fe^{3+} more easily than Japanese cypress wood, owing to its smaller apparent specific gravity. In addition, Japanese cedar wood is much more inexpensive than Japanese cypress wood.

The aim of this study is to investigate the effects of Fe^{3+}-dispersion in wood powder on Fe^0 species yields and graphitization in charcoal, and to elucidate the mechanism of reduction from Fe^{3+} to Fe^0 and graphitization more clearly. Charcoal was synthesized from wood powder prepared using an improved Fe^{3+}-impregnation process under various conditions, and then characterization of iron and carbon in the iron-loaded charcoal was performed using Mössbauer and microscopic Raman spectroscopy. On the basis of the results obtained from the spectroscopic analysis, we discuss the mechanisms of reduction from Fe^{3+} to Fe^0 and graphitization.

Experimental

Preparation of wood powder

Wood chips dried in air for more than 3 months were ground into powder using a cutting-mill. The wood powder, which passed through a 2.0-mm mesh but not through a 1.0-mm mesh, was used for the production of iron-loaded charcoal.

Impregnation with aqueous Fe^{3+} solution

The whole procedures of preparation of iron-loaded charcoal are schematically shown in Fig. 1. Iron(III) nitrate was adopted as an iron salt, because iron nitrates likely produce much less harmful substances than iron halides and sulfates by heat-treatment together with wood. We partly changed the impregnation method from that used in the previous work [10] to enhance the homogeneity of Fe^{3+}-dispersion in wood particles; however, complete homogeneity cannot be accomplished, because wood cell walls, aqueous Fe^{3+} solution absorbent, is a heterogeneous substance chemically and physically. The key change in the impregnation procedure was the addition of a decompression-impregnation process, which is frequently used to make liquid preservatives penetrate

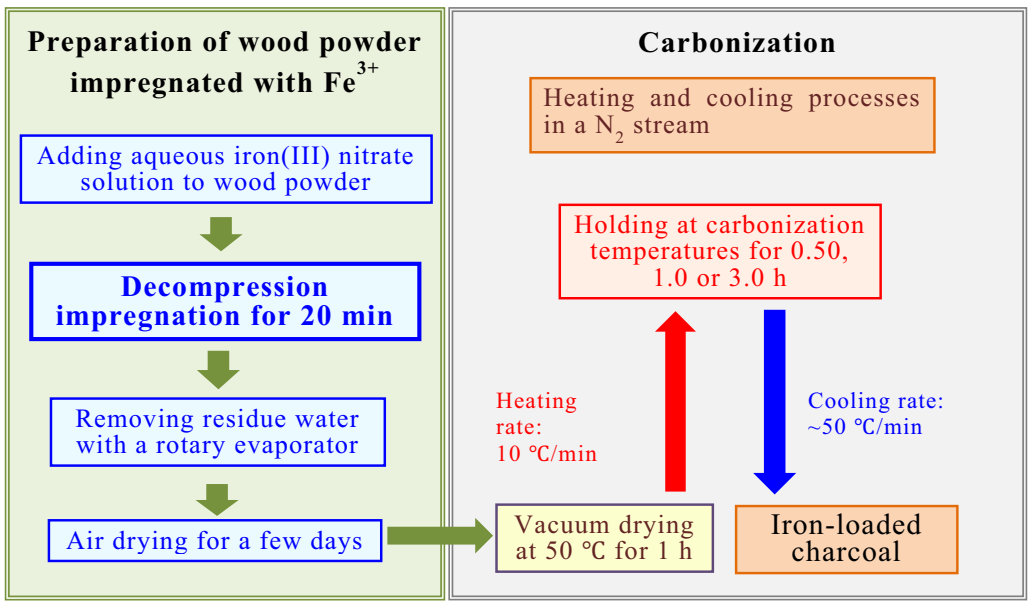

Fig. 1 Flowchart of impregnation with Fe^{3+} and carbonization

into lumber and logs, instead of immersion under atmospheric pressure. It is expected that the air in small cracks of cell wall and cell lumina is removed by the decompression-impregnation. The operation was as follows: wood powder in the Fe^{3+} solution was kept under reduced pressure for 20 min at room temperature in a vacuum desiccator connected to a water-jet pump.

The mass of wood powder after drying at 105 °C for 1.0 h was adopted as the true mass of the wood powder. Fe^{3+} concentrations in the aqueous solution used in this study were set to 0.50 w/w% (solution A) or 0.83 w/w% (solution B). The contents of Fe^{3+} in wood powder were adjusted to be 3 w/w% or 5 w/w% by adding an appropriate amount of the solution A or B, respectively. If necessary, a small amount of water was added to the wood powder in order to immerse it entirely in the solution. The wood powder in the aqueous iron(III) nitrate solution was treated with decompression-impregnation as mentioned above. Excess solvent water was removed from the solution containing wood powder using a rotary evaporator at about 60 °C under reduced pressure and then, the wet wood powder was dried in air for a few days. After evaporation, it was confirmed that no soluble powder remained in a flask connected with the evaporator, indicating that almost all Fe^{3+} ions were absorbed in the wood powder. Thereby, the content of Fe^{3+} in wood were estimated to be 3 w/w% or 5 w/w%.

Carbonization of Fe^{3+}-impregnated wood powder

The block diagrams for carbonization are shown in the right-hand part of Fig. 1. A simplified drawing of the carbonization apparatus used in this study is illustrated in Fig. 2. The Fe^{3+}-impregnated wood powder (~3 g) was placed in a stainless-steel vessel, the bottom of which was made of stainless-steel mesh (mesh opening: 0.84 mm) and the vessel was placed in a round-bottomed flask connected to an oil rotary pump. The flask was heated at 50 °C for 1.0 h under vacuum, and subsequently, the vessel was transferred to a vertical stainless-steel tube reactor. After replacing air with N_2 gas (>99.995%), the reactor was heated to a carbonization temperature (CT; 300 °C, 600 °C, 650 °C, 700 °C, 750 °C, 800 °C, or 850 °C) in a downstream of N_2 gas (1 mL STP cm^{-2} min^{-1}) using an electric furnace; the temperature was increased at a rate of 10 °C/min. The reactor was held at the desired temperature for 0.50 h, 1.0 h or 3.0 h, and subsequently, pulled from the furnace. Ambient-temperature air was blown over the tube reactor using an ordinary air dryer during the cooling period. Cooling rates were estimated to be ~50 °C/min. All carbonization processes, including the cooling process, were carried out under N_2 gas flow. The carbonization procedures used in this study were the same as reported previously [10] when the holding time was set at 1.0 h.

The iron-loaded charcoal samples synthesized from wood are abbreviated as Fe*X*-*Y*-*Z*. The letters of *X*, *Y*, and *Z* are the content (w/w%) of Fe^{3+} in wood, CT, and holding time (HT) at CT, respectively. For example, the charcoal samples made from wood with an Fe^{3+} content of 3 w/w% at 650 °C for 0.50 h is denoted as Fe3-650-0.5. Furthermore, the following abbreviations, which collectively represent a series of charcoal samples, are used as appropriate: Fe3-*Y*-1, Fe3-700-*Z*, Fe*X*-700-1, Fe5-*Y*-1, etc.

Mössbauer spectroscopy

^{57}Fe Mössbauer spectra were recorded in a conventional transmission mode using a Mössbauer spectrometer (Model-222, Topologic System Co., Japan) with a ^{57}Co (Rh) source (925 MBq). Charcoal samples were ground in an agate mortar for a few minutes before Mössbauer measurements. Measurement temperatures were 298 K and 78 K, which were regulated using a cryostat DN-1726 with an ITC-601 temperature controller (Oxford Instruments PLC, UK). The γ-ray transmission diameter of the charcoal sample was ~8 mm. The Mössbauer spectra were analyzed using a curve-fitting processing with the MossWinn 4.0Pre program, assuming that all the spectra were composed of Lorentzian-shaped absorption peaks. The isomer shift (IS) and Doppler velocity scale were calibrated with respect to α-Fe at room temperature.

Raman spectroscopy

Charcoal samples were submitted to Raman measurements after rough grinding. Raman spectra were obtained using a Raman spectrometer (inVia Raman Microscope, Renishaw PLC, UK) with 532 nm laser excitation (0.75 or 1.5 mW). Back-scattered Raman signals were collected through a microscope (50× objective lens) with a spectral resolution of approximately 3 cm^{-1}, and the exposure time was 50 s. Raman measurements were repeated at more than 30 different points for each charcoal sample, because the laser-irradiation point (~2 μm diameter) was too small for sample particle sizes, in which one measurement might lead to a possible deflected result for a sample with inhomogeneity. The calibration of Raman shifts was carried out using the 520 and 1332 cm^{-1} for a silicon wafer and diamond, respectively.

Results and discussion

In this study, Fe3-700-1 and Fe3-850-1 charcoal samples were also synthesized from Japanese cypress wood powder prepared using the improved Fe^{3+}-impregnation method. As a result of Mössbauer and Raman analysis, there were no important differences in iron species yields and graphitization between Fe3-700-1 and Fe3-850-1

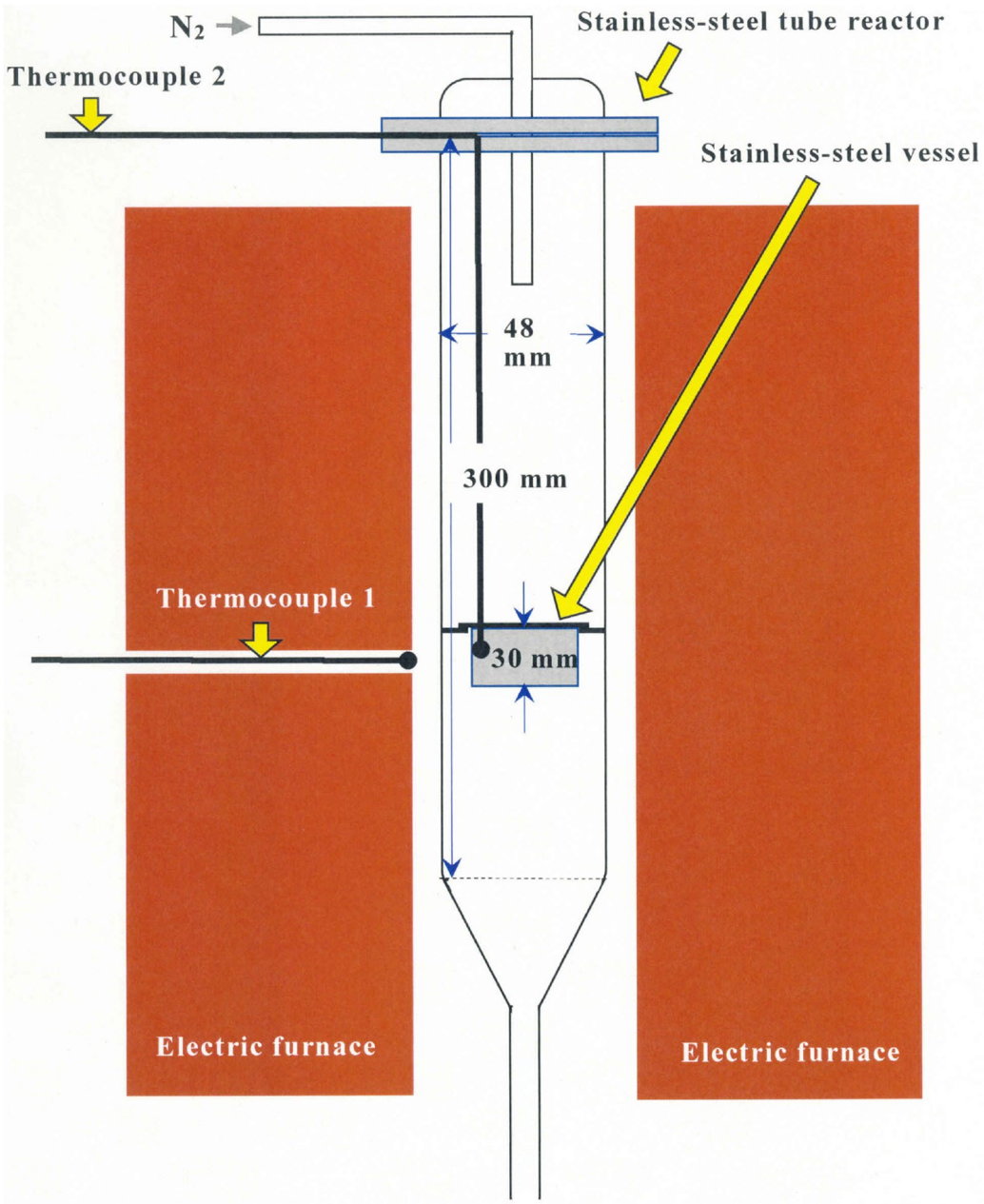

Fig. 2 Schematic diagram of the apparatus for carbonization

samples made from Japanese cedar and Japanese cypress. Thus, we discuss the carbonization of wood impregnated with Fe^{3+}, assuming that Japanese cedar has no significant differences in the properties of iron-loaded charcoal material from Japanese cypress.

Mössbauer spectra of Fe^{3+}-impregnated wood powder

The color of the wood powder turned dark by the impregnation with Fe^{3+}, and the dark color was similar to that of ancient buried Japanese cedar wood containing high contents of multinuclear Fe^{3+}-complexes bonding with functional groups originating from wood constituents [11, 12]. When suspending the air-dried Fe^{3+}-impregnated wood powder in pure water, the aqueous solution turned to brown color while the color of the wood powder was slightly fade out. Thereby, most of the Fe^{3+} ions in wood powder probably formed chemical species of Fe^{3+} soluble in water.

Figure 3 depicts the Mössbauer spectra at 298 K and 78 K of Japanese cedar wood powder impregnated with the Fe^{3+} content of 3 w/w% after the air-drying at room temperature. Both spectra were composed of a doublet and their absorption line-shapes were able to be processed as Lorentzian curves. The parameters obtained using the curve-fitting method are listed in Table 1.

The IS and quadrupole splitting (QS) values at 78 K of the doublet absorption are compatible with those of Fe^{3+} in the ancient Japanese cedar wood [11, 12], revealing that the Fe^{3+} species are most likely present in the high-spin state; however, Fe^{3+} ions in the wood powder are not present in ordinary iron(III) nitrate hydrate of a mononuclear aqua-complex. The Mössbauer absorptions should show a broad and non-Lorentzian singlet line if Fe^{3+} ions form the aqua-complexes [13, 14]. The broadening and deformation from a Lorentzian curve are due to the paramagnetic relaxation effect, and the effect should increase as measurement temperature decreases from 298 to 78 K [15–17]. Actually, the Mössbauer absorptions even at 78 K of the raw wood powder are composed of a Lorentzian doublet, suggesting that high-spin Fe^{3+} ions form multinuclear complexes [18]. Wood constituents having organic functional groups, e.g., hydroxy and carboxy groups, probably crosslink an Fe^{3+} ion with the others, although it is possible that NO_3^- ion also act as a bridging ligand. Accordingly, the Mössbauer data shown in Fig. 3 and Table 1 seem to indicate that the bulk of Fe^{3+} ions enter into the cell walls.

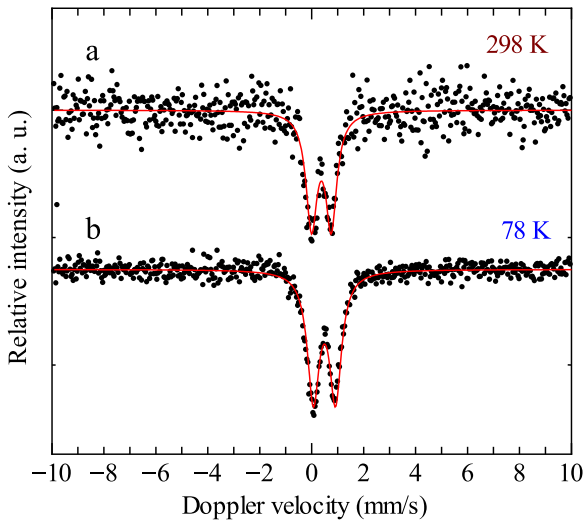

Fig. 3 Mössbauer spectra at 298 K and 78 K of raw Japanese cedar wood impregnated with Fe^{3+} content of 3 w/w%: **a** 298 K, **b** 78 K

In general, a factor governing the efficiency of solid-phase reactions is the uniform dispersion of reactants in the reaction matrix. For example, to disperse the metal atoms as a reactant homogeneously, polymer metal complexes were used as a starting material for making functional carbon [19]. Thus, woody biomass is probably appropriate for a crude material of carbon-based materials made using chemical treatments, because the biomass is able to be impregnated with aqueous and hydrophilic organic solutions.

Mössbauer spectra of Fe3-*Y*-1 charcoal

Figure 4 shows the Mössbauer spectra at 298 K of Fe3-*Y*-1 charcoal samples. The Mössbauer parameters and iron species corresponding to them are summarized in Table 2. As is evident from the figure, the Mössbauer spectra of Fe3-300-1, Fe3-600-1, and Fe3-650-1 are composed of a doublet absorption. Conversely, several components are resolved in the Mössbauer spectra of charcoal samples synthesized at CT of ≥ 700 °C, and some of them are assigned to Fe_3C, α-Fe, or γ-Fe. This is a remarkable result which indicates that most Fe^{3+} ions are reduced to Fe^0 species, i.e., Fe_3C, α-Fe, and γ-Fe, in the CT range from 650 to 700 °C. It should be noted that the CT range is considerably lower than that reported in our previous work [10]. We will discuss such striking fall of the CT range in detail in the later section of this article.

As for Fe3-300-1, Fe3-600-1, and Fe3-650-1, the IS and QS values of their Mössbauer doublet lines are likely assignable to those of high-spin Fe^{3+} species. The high-spin Fe^{3+} species included in Fe3-600-1 and Fe3-650-1 are expected to be nano-sized iron(III) oxide particles as reported previously [10]. According to Gadalla et al. [18], $Fe(NO_3)_3$ hydrates will be decomposed chemically and changed into Fe_2O_3 up to ~ 400 °C. Despite strong internal magnetic fields of α-Fe_2O_3 and γ-Fe_2O_3, no magnetic hyperfine splitting can be observed in the Mössbauer absorptions of Fe3-600-1 and Fe3-650-1, suggesting that Fe_2O_3 particles sizes are so small that a superparamagnetic relaxation phenomenon appears [20].

Table 1 Mössbauer parameters of Japanese cedar wood powder impregnated with Fe^{3+}

Temp. (K)	Type of split	IS (mm/s)	QS (mm/s)	LW (mm/s)	Iron species
298	Doublet	0.37 (1)	0.76 (2)	0.52 (3)	High-spin Fe^{3+}
78	Doublet	0.491 (5)	0.853 (8)	0.55 (1)	High-spin Fe^{3+}

IS isomer shift, *QS* quadrupole splitting, *LW* line width

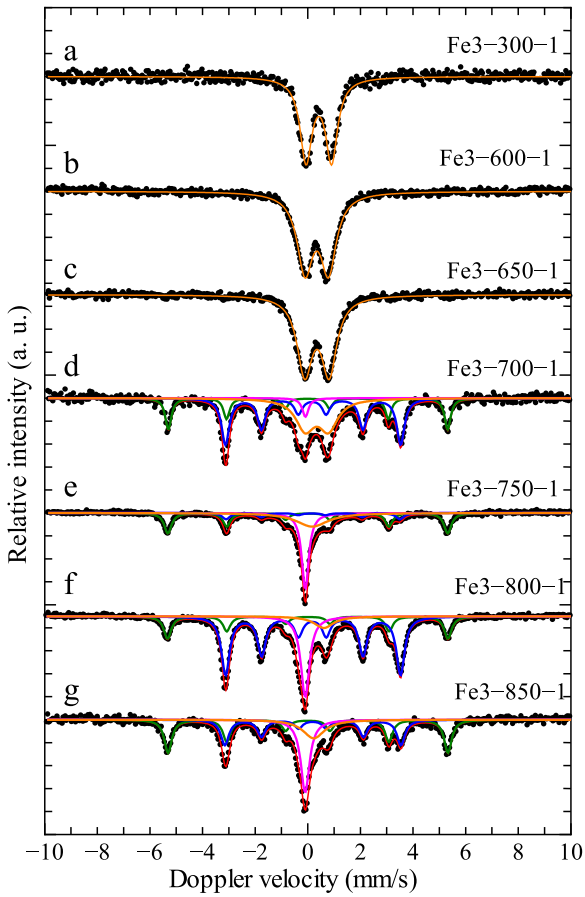

Fig. 4 Mössbauer spectra at 298 K of Fe3-*Y*-1 charcoal samples: **a** Fe3-300-1, **b** Fe3-600-1, **c** Fe3-650-1, **d** Fe3-700-1, **e** Fe3-750-1, **f** Fe3-800-1, **g** Fe3-850-1. Orange solid curve (doublet): high-spin Fe^{3+} species, blue solid curve (sextet 1): Fe_3C, green solid curve (sextet 2): α-Fe, magenta solid curve (singlet): γ-Fe

The Mössbauer spectra of Fe3-300-1 consists of a Lorentzian doublet; however, its IS and QS values are significantly larger compared with those of raw wood powder, Fe3-600-1, and Fe3-650-1. Thus, Fe^{3+} species contained in Fe3-300-1 are likely to be different from the multinuclear complexes in raw wood powder and nano-sized Fe_2O_3 particles in Fe3-600-1 and Fe3-650-1. These Mössbauer parameters may suggest the formation of intermediate iron species before the Fe_2O_3 formation [21].

As shown in Table 2, all Mössbauer spectra of Fe3-*Y*-1 charcoal samples synthesized at ≥ 700 °C are composed of four kinds of components. The three components are attributed to reduced iron species (α-Fe, γ-Fe, and Fe_3C), and the fourth is likely to be assigned to high-spin Fe^{3+} species although this assignment is not completely free from ambiguity. It is noteworthy that the total yield of the reduced iron species reaches 67% when CT is set at 700 °C. This indicates that a rapid increase of the reduction rate from Fe^{3+} to Fe^0 in charcoal occurs in the CT range 650–700 °C, and this range is approximately 150 °C lower than that reported previously [10]. The charcoal samples, which were synthesized from the Fe^{3+}-impregnated wood powder prepared without decompression-impregnation, maintained a considerable amount of high-spin Fe^{3+} species (yield: ~ 80%) when CT was set even at 800 °C, despite the same synthesis conditions in this study other than the Fe^{3+}-impregnation method. As seen in Table 2, the majority of Fe^{3+} species in wood was reduced to Fe^0 at 700 °C, suggesting that addition of the decompression-impregnation process lowered the initial temperature of reduction from Fe^{3+} to Fe^0 remarkably.

Figure 5 illustrates the CT-dependence of iron species yield from 600 to 850 °C. The yield of high-spin Fe^{3+} species decreases with the increase of CT, while those of α-Fe and γ-Fe show an increase tendency with CT from more than 700 °C. The detection of γ-Fe at the measurement temperature of 298 K is explainable in terms of the thermodynamic properties of γ-Fe, which is in a metastable phase, forming only in rapid cooling (~ 50 °C/min) from a higher temperature than the eutectoid transformation temperature of 727 °C [22]; γ-Fe cannot maintain a thermodynamically stable state below this temperature. Further investigations and additional experiment will be required to explain the Fe_3C yield change with CT.

Mössbauer spectra of Fe3-*Y*-*Z* charcoal: effects of HT on iron species yields

Figure 6 depicts the Mössbauer spectra of Fe3-*Y*-*Z* charcoal samples ($Y = 300$ °C, 650 °C, 700 °C and 850 °C; $Z = 0.50$ and 3.0 h), and Table 3 contains a summary of the Mössbauer parameters shown. When wood powder with the Fe^{3+} content of 3 w/w% was carbonized at 300 °C or 650 °C, there was no indication of the presence of reduced iron species in the Mössbauer spectra even though HT was extended by 3.0 h. It should be noted that no Fe^0 species are detected in the Mössbauer spectrum of Fe3-700-0.5, and the spectral line is composed only a doublet showing the IS and QS values close to those of Fe3-600-1 and Fe3-650-1. Conversely, the Mössbauer spectrum of Fe3-700-3 exhibits a similar spectral lineshape to that of Fe3-700-1, indicating that the reduced iron species remain during HT of 3.0 h.

Figure 7 displays the changes in iron species yields with HT for Fe3-700-*Z* and Fe3-850-*Z*, where $Z = 0.50$, 1.0, and 3.0 h. The yield of high-spin Fe^{3+} species in Fe3-700-*Z* decreases drastically and both the yields of Fe_3C and α-Fe increase clearly in the HT range from 0.50 to 1.0 h, although the yields of all the reduced iron (Fe^0) species exhibit no remarkable differences between Fe3-700-1 and Fe3-700-3. In contrast to Fe3-700-*Z* charcoal

Table 2 CT-dependence of Mössbauer parameters at 298 K of iron-loaded charcoal samples

Sample	Type of split	IS (mm/s)	QS (mm/s)	H (T)	LW (mm/s)	Yield (%)	Iron species
Fe3-300-1	Doublet	0.419 (4)	0.971 (7)	–	0.55 (1)	100	High-spin Fe^{3+}
Fe3-600-1	Doublet	0.340 (3)	0.893 (4)	–	0.718 (7)	100	High-spin Fe^{3+}
Fe3-650-1	Doublet	0.348 (2)	0.929 (4)	–	0.699 (7)	100	High-spin Fe^{3+}
Fe3-700-1	Sextet-1	− 0.003 (5)	0 .02 (1)	33.00 (3)	0.28 (1)	22 (1)	α-Fe
	Singlet	− 0.09 (2)	–	–	0.28 (4)	3 (1)	γ-Fe
	Sextet-2	0.185 (3)	0.032 (7)	20.70 (3)	0.36 (1)	42 (1)	Fe_3C
	Doublet	0.34 (1)	0.89 (2)	–	0.86 (4)	33 (1)	High-spin Fe^{3+}
Fe3-750-1	Sextet-1	0.001 (3)	− 0.002 (6)	33.06 (2)	0.334 (8)	34 (1)	α-Fe
	Singlet-1	− 0.095 (1)	–	–	0.321 (7)	30 (1)	γ-Fe
	Sextet-2	0.17 (1)	0.05 (2)	20.54 (8)	0.35 (3)	11 (1)	Fe_3C
	Singlet-2	0.17 (3)	–	–	1.47 (7)	25 (1)	High-spin Fe^{3+}
Fe3-800-1	Sextet-1	0.002 (4)	− 0.008 (7)	33.12 (2)	0.339 (9)	18.8 (4)	α-Fe
	Singlet-1	− 0.098 (2)	–	–	0.400 (6)	20.0 (3)	γ-Fe
	Sextet-2	0.188 (1)	0.026 (3)	20.67 (1)	0.379 (4)	54.7 (4)	Fe_3C
	Singlet-2	0.61 (2)	–	–	0.90 (7)	6.5 (5)	High-spin Fe^{3+}
Fe3-850-1	Sextet-1	0.005 (4)	0.010 (9)	33.07 (3)	0.35 (1)	35 (1)	α-Fe
	Singlet-1	− 0.099 (5)	–	–	0.41 (3)	23 (3)	γ-Fe
	Sextet-2	0.187 (6)	0.02 (1)	20.80 (4)	0.37 (2)	28 (1)	Fe_3C
	Singlet-2	0.22 (8)	–	–	0.99 (8)	14 (4)	High-spin Fe^{3+}

CT carbonization temperature, *IS* isomer shift, *QS* quadrupole splitting, *H* internal magnetic field, *LW* line width

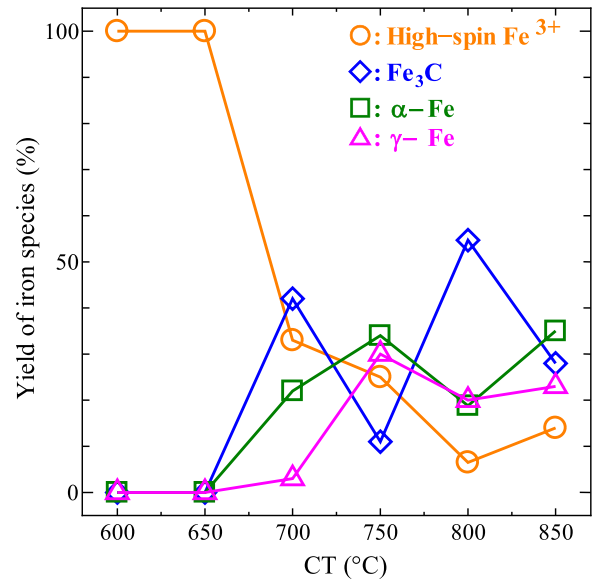

Fig. 5 CT-dependence of iron species yield in Fe3-*Y*-1 charcoal samples. Orange open circle: high-spin Fe^{3+}, blue open rhombus: Fe_3C, green open square: α-Fe, magenta open triangle: γ-Fe

samples, the yield of high-spin Fe^{3+} species is less than 10% in Fe3-850-0.5, and shows little dependence on HT. Similar to the high-spin Fe^{3+} species, the yields of the three reduced iron species exhibit no remarkable changes with HT. These results confirm the suggestion that the reduction reactions of iron are completed virtually up to HT of 0.50 h when CT is set at 850 °C. Moreover, the Mössbauer analysis provides important results which reveal that the re-oxidation of reduced iron species scarcely progresses up to HT of 3.0 h at least, because no magnetic hyperfine splitting due to iron(III) oxides is observed in Fe3-700-3 and Fe3-850-3 charcoal samples.

The appearance of magnetic hyperfine splitting corresponding to Fe_3C and α-Fe in the Mössbauer spectra of Fe3-700-3 and Fe3-850-3 indicates that the two reduced iron species probably formed particles whose sizes were so large that superparamagnetic relaxation effect was negligible [20]. The particle sizes of γ-Fe also seem to be comparable with those of Fe_3C and α-Fe. Hence, if the re-oxidation of reduced iron species proceeds, the produced iron(III) oxides particles should be so large that the Mössbauer spectra of Fe3-700-3 and Fe3-850-3 exhibit magnetic hyperfine splitting assigned to them.

Mössbauer spectra of Fe5-*Y*-1 charcoal: effects of Fe^{3+} content in wood on iron species yields

Figure 8 depicts the Mössbauer spectra of charcoal samples synthesized from the wood powder containing Fe^{3+} of 5 w/w%, and their Mössbauer parameters are summarized in Table 4. It is worthy stressing that Fe5-650-1 charcoal contains Fe_3C and α-Fe of which the yields are 6.2% and 20%, respectively. Whereas the reduction from

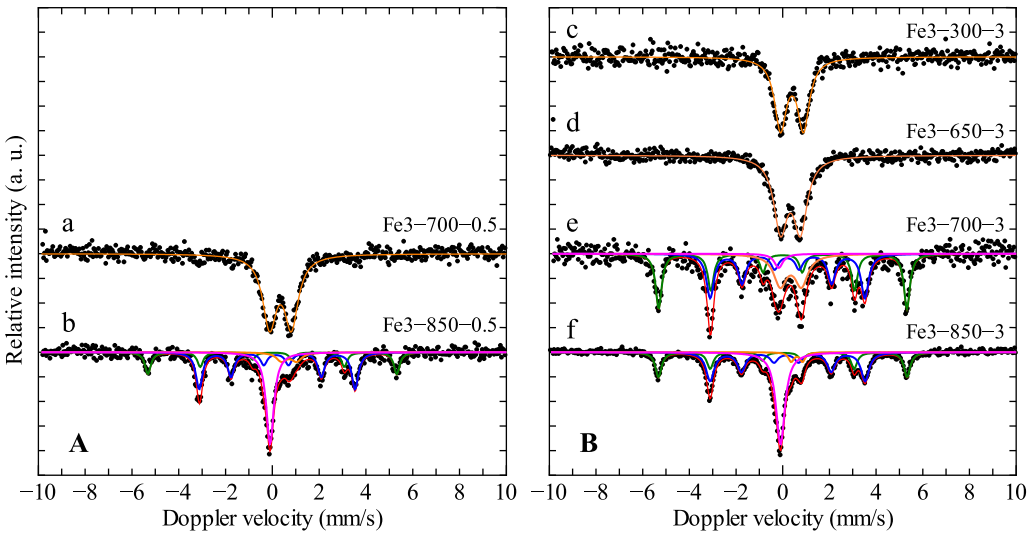

Fig. 6 Mössbauer spectra at 298 K of Fe3-*Y*-*Z* charcoal samples: **A** Fe3-*Y*-0.5 (a, Fe3-700-0.5; b, Fe3-850-0.5); **B** Fe3-*Y*-3 (c, Fe3-300-3; d, Fe3-650-3; e, Fe3-700-3; f, Fe3-850-3). Orange solid curve (doublet): high-spin Fe^{3+} species, blue solid curve (sextet 1): Fe_3C, green solid curve (sextet 2): α-Fe, magenta solid curve (singlet): γ-Fe

Table 3 HT-dependence of Mössbauer parameters at 298 K of iron-loaded charcoal samples

Sample	Type of split	IS (mm/s)	QS (mm/s)	H (T)	LW (mm/s)	Yield (%)	Iron species
Fe3-300-3	Doublet	0.398 (7)	0.99 (1)	–	0.61 (2)	100	High-spin Fe^{3+}
Fe3-650-3	Doublet	0.333 (6)	0.85 (1)	–	0.70 (2)	100	High-spin Fe^{3+}
Fe3-700-0.5	Doublet	0.349 (6)	0.93 (1)	–	0.71 (2)	100	High-spin Fe^{3+}
Fe3-700-3	Sextet-1	0.001 (7)	0.01 (1)	33.06 (4)	0.32 (2)	37 (2)	α-Fe
	Singlet	−0.17 (11)	–	–	0.44 (20)	3 (1)	γ-Fe
	Sextet-2	0.193 (9)	–	20.61 (7)	0.39 (2)	37 (2)	Fe_3C
	Doublet	0.35 (4)	0.91 (7)	–	0.67 (8)	22 (2)	High-spin Fe^{3+}
Fe3-850-0.5	Sextet-1	−0.001 (9)	0.00 (2)	33.06 (6)	0.30 (3)	21 (1)	α-Fe
	Singlet	−0.096 (4)	–	–	0.40 (1)	30 (1)	γ-Fe
	Sextet-2	0.185 (5)	0.041 (11)	20.71 (4)	0.34 (2)	41(1)	Fe_3C
	Doublet	0.72 (5)	0.65 (7)	–	0.54 (13)	8 (1)	High-spin Fe^{3+}
Fe3-850-3	Sextet-1	−0.010 (4)	0.028 (8)	33.11 (2)	0.32 (1)	25 (1)	α-Fe
	Singlet	−0.096 (2)	–	–	0.466 (7)	33.7 (4)	γ-Fe
	Sextet-2	0.181 (4)	0.057 (7)	20.64 (3)	0.414 (9)	37 (1)	Fe_3C
	Doublet	0.61 (1)	0.48 (2)	–	0.28 (3)	4.1 (4)	High-spin Fe^{3+}

HT holding time at CT, *IS* isomer shift, *QS* quadrupole splitting, *H* internal magnetic field, *LW* line width

Fe^{3+} to Fe^0 scarcely proceeds in Fe3-650-*Z* charcoal samples even though HT was extended to 3.0 h, the reduced iron species are clearly observed in the Mössbauer spectrum from Fe5-650-1. Conversely, the yields of the iron species in Fe5-700-1 show no remarkable differences from those in Fe3-700-1, and the same applies for the iron species yields in Fe5-850-1 and Fe3-850-1. These Mössbauer data indicate that the reduction from Fe^{3+} to Fe^0 occurs at lower than 650 °C in the carbonization of wood powder with the Fe^{3+} content of 5 w/w% and the starting temperature of reduction depends upon Fe^{3+} content.

Formation processes of iron species speculated from Mössbauer spectra of iron-loaded charcoal

As mentioned earlier for the explanation of Fig. 4, it is expected that almost all high-spin Fe^{3+} species in Fe3-600-1 and Fe3-650-1 is probably assigned to nano-sized Fe_2O_3 particles. Chemical species displaying the effective reducing power are CO, H_2, and CH_4 among main

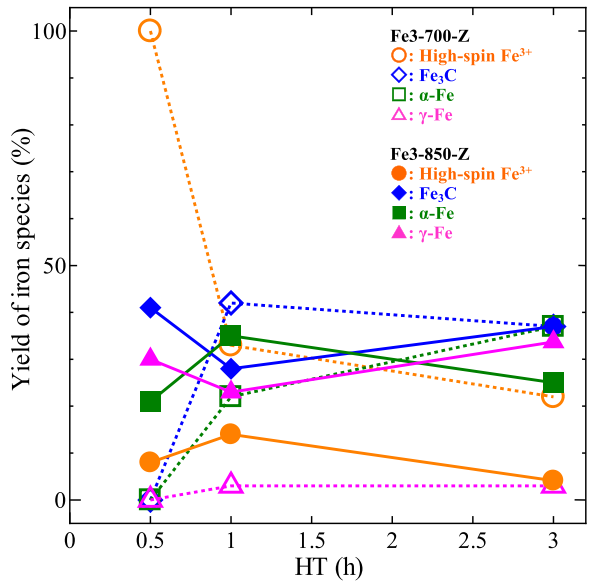

Fig. 7 HT-dependence of iron species yield in Fe3-700-*Z* and Fe3-850-*Z* charcoal samples. Open mark: Fe3-700-*Z* charcoal, full mark: Fe3-850-*Z* charcoal. Orange circle: high-spin Fe^{3+}, blue rhombus: Fe_3C, green square: α-Fe, magenta triangle: γ-Fe

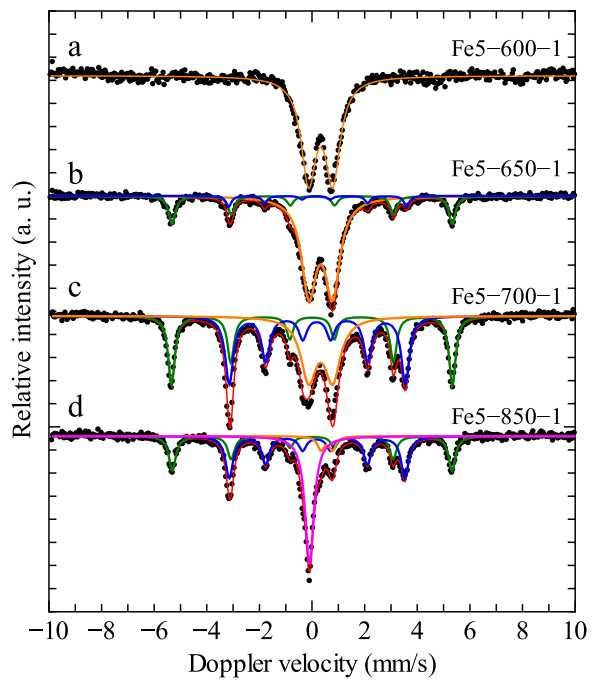

Fig. 8 Mössbauer spectra at 298 K of Fe5-*Y*-1 charcoal samples: **a** Fe5-600-1, **b** Fe5-650-1, **c** Fe5-700-1, **d** Fe3-850-1. Orange solid curve (doublet): high-spin Fe^{3+} species, blue solid curve (sextet 1): Fe_3C, green solid curve (sextet 2): α-Fe, magenta solid curve (singlet): γ-Fe

gases emitted from wood impregnated with Fe^{3+} during the pyrolysis processes [23, 24]. These gases are successively produced from a temperature of < 400 °C during ordinary thermal decomposition of woody biomass [25]. Thus, solid carbon (C) and the three gaseous compounds can act as reductants for Fe_2O_3 in charcoal, and amorphous carbon was generated in charcoal synthesized even at 300 °C, which will be described in details later in the section on Raman spectroscopic results. Based on the reduction mechanism of iron ores accepted generally, the possible reduction reactions are represented as follows:

CO reduction [26, 27]:

$$3Fe_2O_3 + CO \rightarrow 2Fe_3O_4 + CO_2$$

$$Fe_3O_4 + CO \rightarrow 3FeO + CO_2$$

$$FeO + CO \rightarrow Fe + CO_2$$

H_2 reduction [27]:

$$3Fe_2O_3 + H_2 \rightarrow 2Fe_3O_4 + H_2O$$

$$Fe_3O_4 + H_2 \rightarrow 3FeO + H_2O$$

$$FeO + H_2 \rightarrow Fe + H_2O$$

CH_4 reduction [27]:

$$Fe_2O_3 + 3CH_4 \rightarrow 2Fe + 6H_2 + 3O$$

C reduction [26, 27]:

$$3Fe_2O_3 + C \rightarrow 2Fe_3O_4 + CO$$

$$Fe_3O_4 + C \rightarrow 3FeO + CO$$

$$FeO + C \rightarrow Fe + CO$$

In addition, CH_4 conversion and cracking, Fe carburizing (formation of iron carbide), and CO disproportionation reactions will occur during carbonization processes. The whole reduction mechanism in iron-loaded charcoal is presumably composed of the reactions described above and should be complicated; therefore, the contribution of the reductants to Fe_2O_3 reduction is expected to be highly susceptible to carbonization settings.

There occurred no Mössbauer absorptions attributable to Fe_3O_4 or FeO in the spectra of any of the charcoal samples, whereas the formation of Fe_3O_4 and FeO were confirmed in reduced substance from hematite (α-Fe_2O_3) using powder X-ray diffractometry [26, 28, 29]. A possible explanation for no detection of Fe_3O_4 and FeO is that the contents of the intermediate iron oxides remaining in the iron-loaded charcoal submitted to the Mössbauer

Table 4 Mössbauer parameters at 298 K of iron-loaded charcoal samples synthesized from wood containing Fe^{3+} of 5 w/w%

Sample	Type of split	IS (mm/s)	QS (mm/s)	H (T)	LW (mm/s)	Yield (%)	Iron species
Fe5-600-1	Doublet	0.327 (3)	0.918 (5)	–	0.682 (8)	100	High-spin Fe^{3+}
Fe5-650-1	Sextet-1	0.010 (3)	−0.009 (7)	33.11 (2)	0.30 (1)	20 (1)	α-Fe
	Sextet-2	0.185 (8)	0.06 (2)	21.02 (5)	0.24 (2)	6.2 (4)	Fe_3C
	Doublet	0.330 (2)	0.896 (3)	–	0.682 (5)	74.0 (3)	High-spin Fe^{3+}
Fe5-700-1	Sextet-1	−0.001 (2)	−0.005 (3)	33.17 (1)	0.301 (5)	30.7 (4)	α-Fe
	Sextet-2	0.189 (2)	0.022 (4)	20.80 (1)	0.375 (5)	37.1 (4)	Fe_3C
	Doublet	0.327 (4)	0.913 (6)	–	0.72 (1)	32.3 (3)	High-spin Fe^{3+}
Fe5-850-1	Sextet-1	0.004 (4)	0.003 (8)	33.04 (2)	0.31 (1)	26.9 (7)	α-Fe
	Singlet	−0.096 (2)	–	–	0.407 (6)	32.1 (4)	γ-Fe
	Sextet-2	0.181 (3)	0.022 (6)	20.74 (2)	0.349 (8)	35.8 (7)	Fe_3C
	Doublet	0.56 (1)	0.44 (2)	–	0.31 (3)	5.1 (4)	High-spin Fe^{3+}

IS isomer shift, *QS* quadrupole splitting, *H* internal magnetic field, *LW* line width

measurements might be too small to detect them clearly by the measurement in this study. The analytical method other than Mössbauer spectroscopy may be needed to determine whether the intermediate iron oxides are generated in the carbonization procedure.

It is assumed that the four types of reduction occur competitively during the carbonization. Numerous studies on the reductions of Fe_2O_3 have been reported, and most of them discussed the reduction reactions occurring at temperatures higher than 800 °C, which were set based on the reduction of iron ore in a blast furnace. However, several reports provided X-ray diffractometry evidence of the production of metallic iron and Fe_3C from nano-sized Fe_2O_3 powder at lower than 700 °C without a catalyst [26, 28].

Consequently, the remarkable growth of Fe^0 species yield at lower CT is probably caused by the enhancement of the homogeneity of Fe^{3+}-dispersion in wood cell walls, owing to the addition of decompression-impregnation.

Raman spectra of iron-loaded charcoal

Figure 9 shows the typical Raman spectra of Fe3-*Y*-1 charcoal samples. All the Raman spectra exhibit G- and D-bands; moreover, a G′(2D)-band appears in the spectra of charcoal samples synthesized at CT of ≥ 700 °C. These three bands are due to sp^2-carbon; however, the D- and G′-bands are not ordinary Raman bands and their Raman shifts are dependent on the wavelength of the excitation laser. Furthermore, the G′-band is the over tone of the D-band; nevertheless, the intensity of the G′-band is not proportional to that of the D-band. In addition, it is generally recognized that D-band intensity increases as lattice defects in the graphite structure increase [30]. We adopted the G′-band as a marker of graphitic structure formation, assuming that amorphous carbon does not show a G′-band in its Raman spectrum. Furthermore, we qualitatively evaluated the ratio of graphite to amorphous carbon from the ratio of the G′-band intensity to G-band intensity.

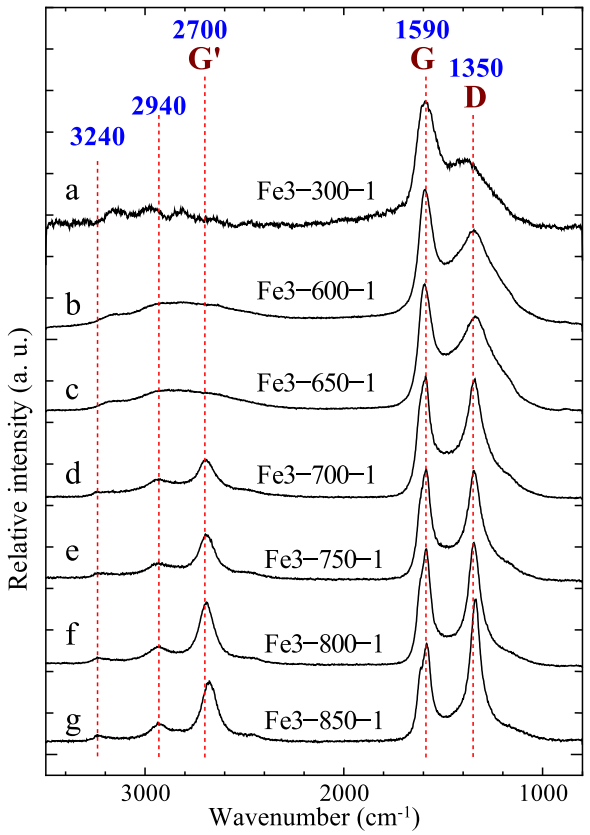

Fig. 9 Typical Raman spectra of Fe3-*Y*-1 charcoal samples: **a** Fe3-300-1, **b** Fe3-600-1, **c** Fe3-650-1, **d** Fe3-700-1, **e** Fe3-750-1, **f** Fe3-800-1, **g** Fe3-850-1

The most noticeable observation obtained from Fig. 9 is changes in spectral line-shape occurring between 650 and 700 °C. This is due mainly to the sharpening of the D-band and appearance of the G′-band, indicating crystallization of sp^2-carbon (i.e., graphitization), and this takes place in the same CT range as the reduced iron species are generated in charcoal samples. Another point worth noting in Fig. 9 is the detection of D- and G-bands in the top Raman spectrum although they are considerably broadened and poorly resolved from each other, suggesting that the formation of chemical bonds involving amorphous sp^2-carbon even at CT of 300 °C. On the other hand, a strong G′-band and sharp D-band are observed in the bottom spectrum of Fe3-850-1, indicating that graphitization progresses quite well. However, it is apparent that the solid carbon even in Fe3-850-1 is far from complete graphitization, comparing with the Raman spectra of high-grade graphite [31, 32].

Although the Raman spectra shown in Fig. 9 are a representative Raman line-shapes of each Fe3-*Y*-1 charcoal sample, measurement-point dependence of the line-shape was observed in Fe3-650-1, Fe3-700-1, and Fe3-750-1, and especially so in Fe3-700-1. Figure 10 depicts the six Raman spectra measured at different points on each charcoal sample. The relative intensity and line-shape of the D-, G-, and G′-bands of Fe3-700-1 largely fluctuates with the measurement point; therefore, the Raman spectrum (Fig. 9d) is an average spectrum of Fe3-700-1 rather than a typical one. A few Raman spectra of Fe3-750-1 as displayed in Fig. 10C-a showed a weaker G′-band as compared with other spectra. As for Fe3-650-1, almost all the Raman spectra showed a broad D-band and no G′-band; however, only a Raman spectrum exhibiting a very weak G′-band was obtained, as shown in Fig. 10A-f.

Interestingly, as shown in Fig. 11, this weak G′-band was observed only at measurement points on pit border (PB) of Fe3-650-1; moreover, the G′-band intensity on the PB tends to be stronger than that on the wall of other parts in the Raman spectra of Fe3-700-1. The results are currently under consideration in terms of the structures and constituents of wood cell walls.

With respect to Fe3-*Y*-1 other than Fe3-650-1, Fe3-700-1, and Fe3-750-1 charcoal samples, the line-shape of the three Raman bands were scarcely changed by the measurement point, although the intensity ratio of the D-band to G-band seems to be slightly dependent on the measurement point on Fe3-800-1 and Fe3-850-1 charcoal samples. Consequently, the Raman spectra of Fe3-*Y*-1 charcoal samples provide further evidence that graphitization is closely related to the reduction from Fe^{3+} to Fe^0 in the carbonization of wood powder impregnated with Fe^{3+}.

Figure 12 depicts the Raman spectra of six different points on Fe3-700-0.5 and Fe3-700-3 charcoal samples. As is evident from the figure, the measurement point influences the Raman spectra of both charcoal samples, especially for Fe3-700-0.5. Approximately half of Raman spectra of Fe3-700-0.5 exhibited little or no G′-band, and the G′-band intensity was weak compared with the typical spectra of Fe3-700-1 even though the band was detected. Conversely, a strong G′-band appeared in almost all the Raman spectra of Fe3-700-3. A point worth noting in Fig. 12A is the detection of the G′-band in several Raman spectra, indicating the formation of graphitic structures in the charcoal.

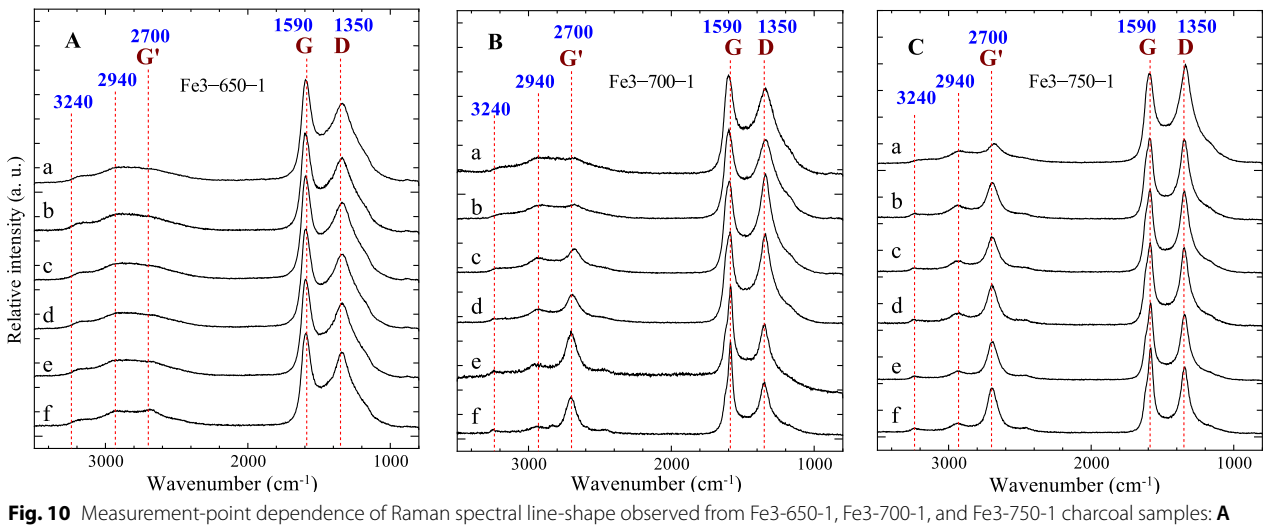

Fig. 10 Measurement-point dependence of Raman spectral line-shape observed from Fe3-650-1, Fe3-700-1, and Fe3-750-1 charcoal samples: **A** Fe3-650-1, **B** Fe3-700-1, **C** Fe3-750-1

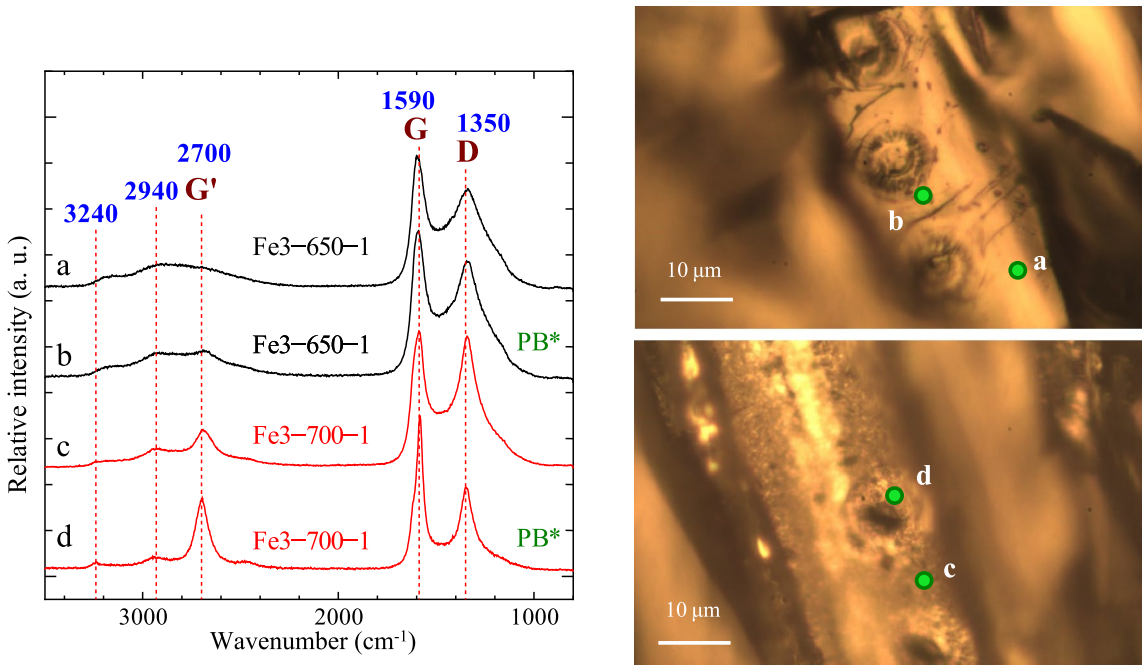

Fig. 11 Cell-wall site dependence of the relative G′-band intensity observed from Fe3-650-1 and Fe3-700-1 charcoal samples: **a** ordinary wall of Fe3-650-1; **b** pit border of Fe3-650-1; **c** ordinary wall of Fe3-700-1; **d** pit border of Fe3-700-1. *PB** pit border

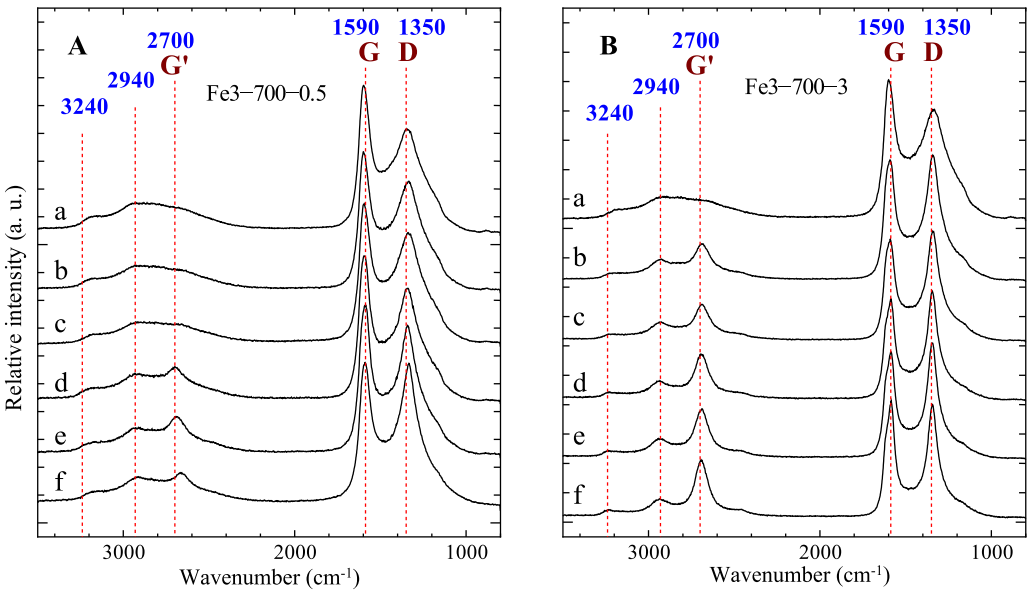

Fig. 12 Measurement-point dependence of Raman spectral line-shape observed from Fe3-700-0.5 and Fe3-700-3 charcoal samples: **A** Fe3-700-0.5, **B** Fe3-700-3

Figure 13 displays the typical Raman spectra of Fe5-*Y*-1 charcoal samples. The Raman spectra of these charcoal samples show the same CT-dependence as that of Fe3-*Y*-1. In other words, a critical spectral change was observed in the CT range from 650 to 700 °C. It should be noted that no G′-band was found in Fe5-650-1 charcoal despite more than 100 different point-measurements containing the pit border.

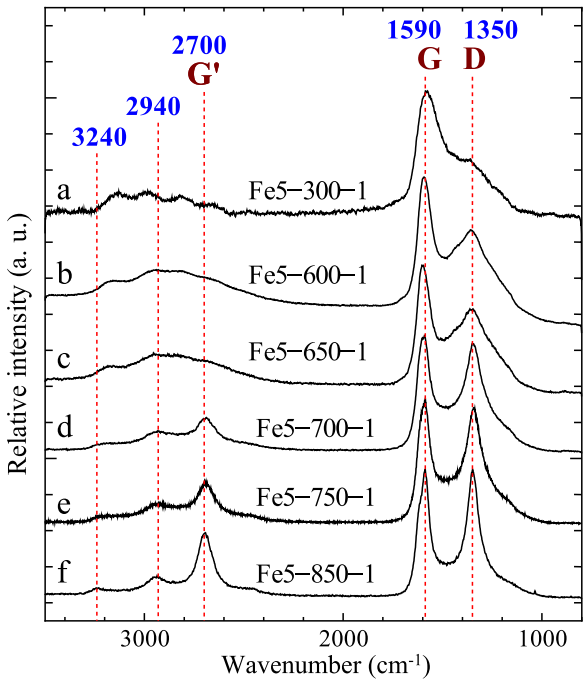

Fig. 13 Typical Raman spectra of Fe5-*Y*-1 charcoal samples: **a** Fe5-300-1, **b** Fe5-600-1, **c** Fe5-650-1, **d** Fe5-700-1, **e** Fe5-750-1, **f** Fe5-850-1

Graphitization mechanism deduced from Mössbauer and Raman data

We comprehensively discuss the relationship between the reduction from Fe^{3+} to Fe^0 and graphitization in the carbonization of wood powder impregnated with Fe^{3+}, based on the results obtained from the Mössbauer and Raman spectroscopic characterization.

We previously reported that both reduction and graphitization progressed rapidly from 800 to 850 °C [10]. Nevertheless, the Mössbauer and Raman measurements in this study indicate that rapid progress occurs in the CT range of 650–700 °C. As mentioned above, this difference for the critical CT range is probably attributable to improvement in Fe^{3+}-impregnation. In particular, it is presumed that Fe^{3+} ions are dispersed more homogeneously in wood cell walls, owing to the addition of decompression-impregnation, and thereby, the starting temperature of Fe^{3+}-reduction is greatly reduced.

Here, a key issue that should be discussed based on the spectroscopic characterization is the chronological order of the reduction from Fe^{3+} to Fe^0 and graphitization in the carbonization process. In other words, it is necessary to find clues to determine which reactions occur earlier, reduction or graphitization. A few studies have been published on graphitization in carbon-based materials containing iron and nitrogen [33, 34] or metallic iron–amorphous carbon systems [35, 36], and they have individually proposed a hypothesis on the mechanism of graphitic structure formation on the basis of experimental evidence. All of them provide a cogent, scientific explanation for the mechanism of graphitization involving iron; however, it is likely to be difficult to explain graphitization completely in complex systems such as iron-loaded charcoal using a reaction path alone.

The graphitization mechanisms with iron reported previously have been explained in the two following ways:

1. Metallic iron and Fe_3C, which are Fe^0 species, start to graphitize amorphous carbon. In other words, Fe^0 species play a role as a catalyst for graphitization [36].
2. Iron forms intermediate species prior to the reduction to Fe^0, and these species contribute to construct graphite structures [33, 34].

The reduction from Fe^{3+} to Fe^0 must occur before the formation of graphitic structures even if partly when the mechanism (1) is solely applied to this study. The absorptions due to Fe^0 species appear weakly but clearly in the Mössbauer spectrum of Fe5-650-1 (Fig. 8b); however, no Raman scattering assigned to the G′-band was detected despite more than 100 different point-measurements, and the first detection of the G′-band was confirmed in Fe5-700-1. Thus, the Mössbauer and Raman spectroscopic data for Fe5-*Y*-1 charcoal can be explained using the mechanism (1). Moreover, as for Fe3-*Y*-1 charcoal, both Fe^0 species and graphite structure were confirmed in the samples synthesized at $\geq$700 °C, although a very weak G′-band was detected at only two measurement points among more than 50 in Fe3-650-1 despite observation of no Fe^0 species. Hence, it is likely that both the Mössbauer and Raman spectroscopic analyses of Fe3-*Y*-1 charcoal are not inconsistent with the mechanism (1). However, whereas the appearance of the G′-band was confirmed in a number of Raman spectra of Fe3-700-0.5 (Fig. 12A), neither absorptions due to α-Fe nor Fe_3C were observed in the Mössbauer spectrum (Fig. 6c). It is difficult to account for the results for Fe3-700-0.5 without contradiction only using mechanism (1), even assuming that the Mössbauer doublet contains the absorptions due to trace amounts of nano-sized α-Fe or Fe_3C particles showing no magnetic hyperfine splitting.

Similarly, it is difficult for the mechanism (2) by itself to explain all the Mössbauer and Raman results for the following reasons. First, although the G′-band is expected to be observed in the Raman spectra of Fe*X*-650-*Z* at least because graphitic structures should be formed before the production of Fe^0 species, no solid G′-band was detected (Figs. 10A and 13c). Second, no

absorptions attributable to intermediate iron species were found in the Mössbauer spectra of any charcoal samples.

Various chemical reactions and physical changes (e.g., pyrolysis of wood, redox of iron, crystallization, aggregation, and diffusion) should progress competitively in the carbonization of the complicated materials used in this study. It can be presumed that there are multiple reaction paths to graphitization and the main path easily switches with others depending on the carbonization conditions. With respect to the charcoal samples synthesized at ≥ 750 °C, it may be expected that Fe^0 species provide strong support for graphitization. However, other mechanisms of graphitization are required for the carbonization in the critical CT range of 600–700 °C. Thus, we could have a hypothesis that Fe_3O_4 and/or FeO also develop graphitic structures, although the formation of the intermediate iron oxides has not been observed experimentally. In addition, graphitization might not progress smoothly until functional groups and molecular frameworks originated from wood constituents are almost pyrolyzed, even if Fe^0 species and amorphous sp^2-carbon were generated in charcoal. Further study and insights are necessary to elucidate the mechanisms of reduction from Fe^{3+} to Fe^0 and graphitization more clearly.

Conclusion

The Mössbauer and Raman spectroscopic characterization of iron-loaded charcoal carbonized using the improved Fe^{3+}-impregnation method provided the important information about the carbonization of wood impregnated with Fe^{3+}.

We conclude that the generation of Fe^0 species at the lower CT range of 600–700 °C is attributed to enhancement of the homogeneity of Fe^{3+}-dispersion in wood cell walls. It can be presumed that more homogeneous dispersion of Fe^{3+} ions makes the Fe_2O_3 particle-size smaller, and thereby the reduction of Fe_2O_3 occurs smoothly.

The results obtained from the Mössbauer and Raman measurements indicated that carbonization reactions are complicated and cannot be comprehensively explained using a simple model. However, it is likely that Fe^0 species provide strong support for graphitization when CT and HT are set at ≥ 750 °C and ≥ 1.0 h, respectively. Moreover, multiple possible reaction paths to graphitization are expected to be included in the whole carbonization process, and the primary path might be readily exchangeable for others depending on the carbonization settings.

Abbreviations

CT: Carbonization temperature; HT: Holding time; IS: Isomer shift; QS: Quadrupole splitting; LW: Line width; PB: Pit boarder; Fe*X*-*Y*-*Z*: The letters of *X*, *Y*, and *Z* are the content (w/w%) of Fe^{3+} in wood, CT, and HT, respectively.

Acknowledgements

Not applicable.

Authors' contributions

TY and SY designed this study, and wrote the initial draft of the manuscript. HS and SS prepared the iron-loaded charcoal samples. SY performed Raman spectroscopic analysis. YS and TT were major contributors in obtaining and analyzing Mössbauer spectra. All authors have contributed to data collection and interpretation, and critically reviewed the manuscript. All authors read and approved the final manuscript.

Funding

This work was partly supported by a Grant-in Aid for Scientific Research (Grant Number 21K05714) from the Japan Society for the Promotion of Science.

Availability of data and materials

The datasets used and analyzed in the current study are available from the corresponding author on reasonable request.

Declarations

Competing interests

The authors declare that they have no competing interests.

Author details

[1]Department of Applied Chemistry, The University of Tokyo, 7-3-1 Hongo, Tokyo 113-0033, Japan. [2]Institute of Wood Technology, Akita Prefectural University, 11-1 Kaieisaka, Noshiro 016-0876, Japan. [3]Department of Chemistry, Daido University, Takiharu-Cho, Minami-ku, Nagoya 457-8530, Japan.

Received: 12 July 2021 Accepted: 30 January 2022
Published online: 12 February 2022

References

1. Suzuki K, Suzuki T, Takahashi Y, Okimoto M, Yamada T, Okazaki N, Shimizu Y, Fujiwara M (2005) Preparation of crystallized and mesoporous carbon by nickel-catalyzed carbonization of wood. Chem Lett 34:870–871
2. Suzuki T, Suzuki K, Takahashi Y, Okimoto M, Yamada T, Okazaki N, Shimizu Y, Fujiwara M (2007) Nickel-catalyzed carbonation of wood for coproduction of functional carbon and fluid fuels I: production of crystallized mesoporous carbon. J Wood Sci 53:54–60
3. Suzuki T, Suzuki K, Saito Y, Yasui S, Okazaki N, Yamada T (2008) High electroconductivity of wood char obtained by iron-catalyzed carbonation. Chem Lett 37:798–799
4. Suzuki K, Suzuki T, Takahashi Y, Okimoto M, Yamada T, Okazaki N, Shimizu Y, Fujiwara M (2009) Nickel-catalyzed carbonization of wood for coproduction of functional carbon and fluid fuels II: improved fuel quality of oil fraction and increased heating value of gas fraction. J Wood Sci 55:60–68
5. Suzuki T, Shinomoto T, Matsuzaki H, Suzuki K, Okazaki N, Saito Y, Kita H, Tamai H (2011) Production of functional carbon by iron-catalyzed carbonation of biomass-effect of washing with acid followed by atmospheric oxidation on the electroconductivity of crystallized mesoporous wood carbon. Trans Mat Res Soc Jpn 36:417–420
6. Kodama Y, Sato K, Suzuki K, Saito Y, Suzuki T, Konno TJ (2012) Electron microscope study of the formation of graphitic nanostructures in nickel-loaded wood char. Carbon 50:3486–3496
7. Suzuki K, Suzuki T, Hattori K, Okazaki N, Saito Y, Kita H, Tamai H (2012) Liquid phase adsorption of dyes and dextrans by crystallized mesoporous wood carbon obtained by nickel-catalyzed carbonization of larch at 900 °C. Wood Carbonization Res 9:21–29

8. Suzuki K, Saito Y, Kita H, Sato K, Konno T, Suzuki T (2017) Production of carbon nanoshell chains by the co-catalyzed carbonization of wood. TANSO No. 277, pp 55–62
9. Suzuki K, Saito Y, Okazaki N, Suzuki T (2020) Graphite-shell-chains selectively and efficiently produced from biomass rich in cellulose and chitin. Sci Rep 10:12131. https://doi.org/10.1038/s41598-020-69156-y
10. Yamagishi T, Yamauchi S, Suzuki K, Suzuki T, Kurimoto Y, Takayama T, Yoichi S (2020) Mössbauer and Raman spectroscopic characterization of iron and carbon in iron-loaded Japanese cypress charcoal. J Wood Sci 66:82–87. https://doi.org/10.1186/s10086-020-01930-y
11. Yamauchi S, Kurimoto Y, Sakai Y (2017) Mössbauer characterization of iron in ancient buried trees excavated from the foothills of Mt. Chokai. J Nucl Radiochem Sci 17:23–29
12. Kurimoto Y, Yamauchi S, Takayama T, Sakai Y (2020) Coloring mechanisms of ancient buried wood: Japanese cedar trees excavated from the foothills of Mt. Chokai. J Wood Sci 66:24–29. https://doi.org/10.1186/s10086-020-01870-7
13. Housley RM (1967) Investigation of magnetic relaxation effects in $Fe(NO_3)_3{\cdot}9H_2O$ and $NH_4Fe(SO_4)_2{\cdot}12H_2O$ by Mössbauer spectroscopy. J Appl Phys 38:1287–1289
14. Sontheimer F, Nagy DL, Dézy I, Lohner T, Ritter G, Seyboth D, Wegener H (1974) Spin relaxation effects in $Fe(NO_3)_3$ and $Fe(ClO_4)_3$ frozen solutions and in $Fe(ClO4)_3$ crystal hydrates. J Physique 35C6:443–448
15. Yamauchi S, Sakai Y, Nishioji H, Tominaga T (1983) Mössbauer spectroscopic study of the magnetic relaxation in tris(β-diketonato) iron(III) complexes. Int J Appl Radiat Isot 34:977–979
16. Yamauchi S, Sakai Y, Tominaga T (1985) Mössbauer spectroscopic studies of the correlation between molecular structure and sign of quadrupole splitting in tris(β-diketonato) iron(III) complexes utilizing paramagnetic relaxation effects. Bull Chem Soc Jpn 58:442–446
17. Yamauchi S, Sakai Y, Tominaga T (1987) Paramagnetic relaxation effects on Mössbauer spectra of hexakis(alkylurea) iron(III) complexes. J Radioanal Nucl Chem Lett 119:283–289
18. Yamauchi S, Kurimoto K, Sakai Y (2017) Mössbauer characterization of Iron in the ancient buried trees excavated from the foothills of Mt. Chokai. J Nucl Radiochem Sci 17:23–29
19. Kobayashi M, Niwa H, Saito M, Harada Y, Oshima M, Ofuchi H, Terakura K, Ikeda T, Koshigoe Y, Ozaki J, Miyata S (2012) Indirect contribution of transition metal towards oxygen reduction reaction activity in iron phthalocyanine-based carbon catalysts for polymer electrolyte fuel cells. Electrochim Acta 74:254–259
20. Nasu S (2013) General introduction to Mössbauer spectroscopy, chap 1. In: Yoshida Y, Langouche G (eds) Mössbauer spectroscopy. Springer, Berlin, pp 1–22
21. Melnikov P, Nascimento VA, Arkhangelsky IV, Zanoni Consolo LZ, De Oliveira LCS (2014) Thermal decomposition mechanism of iron(III) nitrate and characterization of intermediate products by the technique of computerized modeling. J Therm Anal Calorim 115:145–151
22. Okamoto H (1992) The C-Fe (carbon-iron) system. J Phase Equilibria 13:543–565
23. Suzuki K, Suzuki T, Takahashi Y, Okimoto M, Yamada T, Okazaki N, Shimizu Y, Fujiwara M (2009) Nickel-catalyzed carbonization of wood for coproduction of functional carbon and fluid fuel II: improved fuel quality of oil fraction and heating value of gas fraction. J Wood Sci 55:60–68
24. Eibner S, Broust F, Blin J, Julbe A (2015) Catalytic effect of metal nitrate salts during pyrolysis of impregnated biomass. J Anal Appl Pyrolysis 113:143–152
25. Li H, Li W, Ji Y, Xue S, Wang Z (2019) Study on the mechanism of gas component release for biomass pyrolysis. In: Paper presented at 4th International conference on advances in energy and environment research, Shanghai University of Electric Power, Shanghai, 16–18 August 2019
26. Kawanari M, Matsumoto A, Ashida R, Miura K (2011) Enhancement of reduction rate of iron ore by utilizing iron ore/carbon composite consisting of fine iron ore particles and highly thermoplastic carbon material. ISIJ Int 51:1227–1233
27. Sun G, Li B, Guo H, Yang W, Li S, Guo J (2020) Thermodynamic study on reduction of iron oxides by $H_2 + CO + CH_4 + N_2$ mixture at 900 °C. Energies 13:5053–5070
28. Hisa M, Tsutsumi A, Akiyama T (2004) Production of iron oxides by nano-sized particles observed in pre-oxidized iron carbide at temperatures around 873 K. Mat Trans 45:1907–1910
29. Chen Z, Dang J, Hu X, Yan H (2018) Reduction kinetics of hematite powder in hydrogen atmosphere at moderate temperatures. Metals 8:751–760
30. Pimenta MA, Dresselhaus G, Cançado LG, Jorio A, Saito R (2007) Studying disorder in graphite-based systems by Raman spectroscopy. Phys Chem Chem Phys 9:1276–1294
31. Ferrari AC (2007) Raman spectroscopy of graphene and graphite: disorder, electron–phonon coupling, doping and nonadiabatic effects. Solid State Commun 143:47–57
32. Zólyomi V, Koltai J, Kürti J (2011) Resonance Raman spectroscopy of graphite and graphene. Phys Status Solidi B 248:2435–2444
33. Charreteur F, Jaouen F, Ruggeri S, Dodelet J-P (2008) Fe/N/C non-precious catalysis for PEM fuel cells: influence of the structural parameters of pristine commercial carbon blacks on their activity for oxygen reduction. Electrochim Acta 53:2925–2938
34. Singh D, Tian J, Mamtani K, King J, Miller JT, Ozkan US (2014) A comparison of N-containing carbon nanostructures (CNx) and N-coordinated iron-carbon catalysis (FeNC) for the oxygen reduction reaction in acidic media. J Catalysis 314:30–43
35. Bokhonov B, Korchagin M (2002) The formation of graphite encapsulated metal nanoparticles during mechanical activation and annealing of soot with iron and nickel. J Alloy Compd 333:308–320
36. Anton R (2009) In situ TEM investigations of reactions of Ni, Fe and Fe–Ni alloy particles and their oxides with amorphous carbon. Carbon 47:856–865

Publisher's Note